ARTICLE OPEN

Phase transition and electrical conversion properties of Ge/Sb nano-multilayer films on flexible substrates

Cheng Wang [1], Yifeng Hu [1,2,3]✉ and Li Li [2,3]

Flexible information memory is the key component of flexible electronic devices and the core of intelligent wearable devices. In this paper, Ge/Sb multilayer phase change films of various thickness ratios were prepared using polyether ether ketone as substrate, and their flexible phase change properties and device conversion characteristics were studied. After bending for 100000 times and bending experiments with different bending radius, the film can still realize the transition from amorphous to crystalline states, and the resistance fluctuation was small. Bending, stretching and pressing of the film resulted in grain refinement and increasing of crystalline resistance. The flexible electronic devices using Ge/Sb multilayer films were prepared. The phase change memory device can realize reversible conversion between SET and RESET states with different pulse widths in flat, bent states and after bending many times. All findings show that Ge/Sb multilayer films on PEEK substrate have broad application prospects in high-performance flexible memory in the future.

npj Flexible Electronics (2024)8:8 ; https://doi.org/10.1038/s41528-024-00296-1

INTRODUCTION

With the rise of smart healthcare devices and wearable technology, flexible electronic devices have gradually become the focus of attention[1–3]. As the core of intelligent electronic equipment, information memory is developing towards low power consumption and flexibility[4]. Flexible materials can be deformed to adapt to various application environments, making flexible electronic devices easier to carry and use than traditional rigid devices[5,6]. The traditional Si substrate is hard to be integrated into flexible electronic devices and adapted to the working environment that needs deformation due to the limitation of bending[7–9]. Therefore, it is necessary to develop memory based on flexible substrate to advance the development of high-performance flexible electronic devices in the future.

In contrast to volatile memory, non-volatile memory can retain data for a long time without the need for continuous power supply[10,11]. The existing non-volatile memory includes Flash memory (Flash), phase change memory (PCM), magnetic memory (MRAM), ferroelectric memory (FeRAM) and resistive memory (RRAM)[12–17]. PCM has the characteristics of fast read and write speed, high data density, long life, low power consumption, scalability and high reliability[18,19]. During the writing operation, the phase change material can be changed from amorphous to crystalline states by applying a weak current pulse. When the operation is resumed, a strong current pulse is applied to rapidly heat the phase change material to an amorphous state. According to the resistance state of the material, it is possible to determine whether the stored data is "0" or "1"[20–25]. Based on the above advantages, PCM has become a candidate for the next generation memory, and has broad development prospects in various applications. The flexible substrate material is the key to the development of flexible PCM, which must have the characteristics of high temperature resistance, strong bending fatigue resistance and insulation[26–31]. Flexible polyether ether ketone (PEEK), as an engineering material with excellent performance, has the characteristics of high temperature stability (melting point ~334 °C), good fatigue and bending strength, corrosion resistance, strong insulation and good biocompatibility[32]. Compared with the PET flexible substrate, the thermal deformation temperature of PEEK substrate is 260 °C, and the thermal deformation temperature of PET substrate is only 80 °C, so PEEK substrate has good thermal stability and mechanical properties. Due to its excellent performance, PEEK is now widely used in aerospace, medical, automotive, electronics and chemical industries, and is potential to become the substrate for future flexible memory[33].

The references show that Sb phase change material is the optimal material for high speed PCM because of its simple structure, nucleation and low crystallization temperature[34]. In order to further improve the thermal stability of Sb phase change materials, the nanoscale composite of Ge material and Sb was carried out by stacking multiple layers. Ge/Sb multilayer films were prepared on flexible PEEK substrate by magnetron sputtering technology. The phase transformation properties, resistance drift, microstructure, surface morphology and electrical properties of Ge/Sb multilayer films with PEEK as substrate were investigated. The experimental results show that the Ge/Sb multilayer film prepared on PEEK have excellent thermal stability, anti-bending cycle, anti-stretching, anti-pressure and electrical performance, and can be used for future flexible phase-change memory materials.

RESULTS AND DISCUSSION

Thermal stability testing of flexible Ge/Sb films

Figure 1a depicts a schematic diagram of a hot and cold table test system for measuring the film resistance-temperature (*R*–*T*) relationship. The test system is composed of temperature controller, megger, heating table and computer. The temperature controller controls the temperature of the heating table, tests the resistance change of the film in the process of temperature change, and finally *R*–*T* curves are generated for each film on the computer. As shown in Fig. 1b, Ge/Sb multilayer films with different thickness ratios on a flexible PEEK substrate exhibited an amorphous state at first when heated at a rate of 20 °C min^{-1}. Resistance slowly decreased with increasing temperature until it reached a specific value known as phase transition

[1]School of Mathematics and Physics, Jiangsu University of Technology, Changzhou 213000, China. [2]Jincheng Research Institute of Opo-mechatronics Jincheng, 48000 Jincheng, China. [3]Shanxi Key Laboratory of Advanced Semiconductor Optoelectronic Devices and Integrated Systems, Jincheng 48000, China. ✉email: hyf@jsut.edu.cn

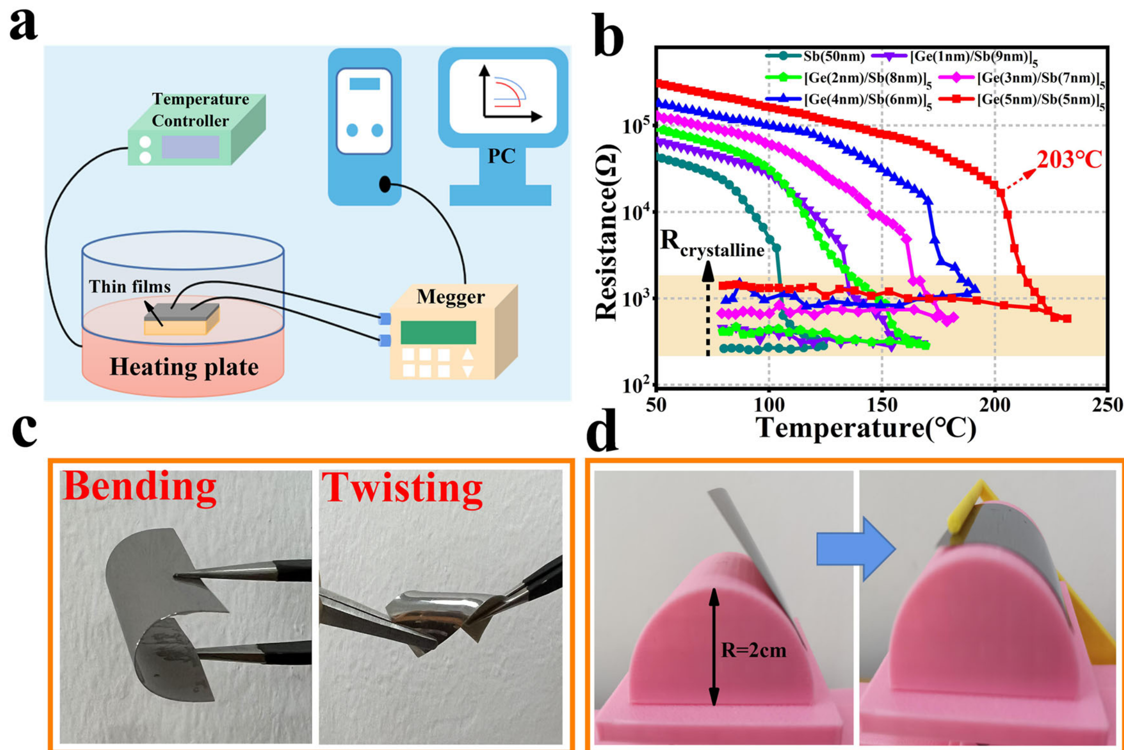

Fig. 1 Thermal stability test and bending device diagram. **a** Schematic diagram of the test system for hot and cold stations. **b** *R*–*T* relationship curves of Ge/Sb multilayer films with different thickness ratios on PEEK substrate. **c** Physical drawings of bending and twisting states of flexible PEEK films; **d** Physical diagram of the bending process of [Ge(5 nm)/Sb(5 nm)]$_5$ multilayer film on the bending model with PEEK as the substrate.

temperature T_c where resistance plummeted sharply[35]. The resistance of the film is stable at a low value during the cooling process, which indicates that the film has completed the transition from amorphous to crystalline states. The observed changes in amorphous and crystalline resistances are more than two orders of magnitude, indicating that phase transition is feasible for Ge/Sb multilayer films on flexible PEEK substrates. With the increase of Ge content, the T_c of Ge/Sb films also increases and is higher than that of single-layer Sb (50 nm) films. The T_c of [Ge(5 nm)/Sb(5 nm)]$_5$ multilayer films is as high as 203 °C, which demonstrates that the addition of Ge layers has been found to enhance the thermal stability of the films. In addition, as the Ge layer thickness increases, the crystalline resistance of the film increases from 263 Ω of the single-layer Sb film to 1408 Ω of the [Ge(5 nm)/Sb(5 nm)]$_5$ multilayer film, which can contribute to reducing the drive current of the PCM device during the reset operation[36].

Figure 1c displays the pictures of a Ge/Sb multilayer film with flexible PEEK as the substrate in bent and twisted state. After bending and twisting operation, Ge/Sb multilayer film can still adhere to the substrate well, indicating that it has good flexibility. Figure 1d shows the bending process of the [Ge(5 nm)/Sb(5 nm)]$_5$ multilayer film on the bending model with PEEK as the substrate. In order to ensure the same bending stress at all locations of the film during the bending process, we fix one end of the film on a 3D model with a radius of 20 mm, and then set the bending frequency to 1 time/s on the bending cycle device, and the number of bending cycles can be set arbitrarily. After activating the bending cycle device, the other end of the film is attached to the 3D model and then released, ensuring that the bending radius of all locations on the film is 20 mm, thus ensuring that the bending stress is consistent at all locations of the film.

Figure 2a displays the *R*–*T* graphs of the [Ge(5 nm)/Sb(5 nm)]$_5$ multilayer film on PEEK substrate after 10^5 cycles from flat to bending states. It can be seen from the figure that [Ge(5 nm)/Sb(5 nm)]$_5$ multilayer film still has good phase transition performance after bending on PEEK substrate for many times, indicating that the film has excellent bending fatigue resistance. In Fig. 2a, the amorphous and crystalline resistance values and phase transition temperature of the film at 85 °C after multiple bending were collected and plotted in Fig. 2b. From the data presented in Fig. 2b, it is evident that with the increase of bending cycles, the difference between amorphous and crystalline resistance of the film remains at two orders of magnitude, which is conducive to the accurate identification of data states. In addition, after multiple bending, the resistance values of the film both in amorphous and crystalline states exhibit a slight increase, which may be because the effective cross section through which the current passes is reduced by bending. Figure 2b also shows that the phase transition temperature drops from 203 °C in the flat state to 184 °C after 10^5 bending times. The decrease in thermal stability of the film may be attributed to the disruption of its internal structure and the emergence of multiple imperfections[37].

Figure 2c displays the *R*–*T* graphs of the [Ge(5 nm)/Sb(5 nm)]$_5$ multilayer film on PEEK substrate after 10^4 bending times with different bending radius. The bending model is illustrated in Fig. 2d with bending radius of 1.0, 1.5, 2.0, 2.5 and 3.0 cm respectively. As can be seen from Fig. 2c, all [Ge(5 nm)/Sb(5 nm)]$_5$ films exhibit obvious amorphous to crystalline phase transition behavior at different bending radius. The amorphous and crystalline resistance values after bending at different bending radius are collected in Fig. 2c and plotted in Fig. 2d. It can be seen that after the film is bent 10^4 times at different bending radius, the amorphous and crystalline resistance values remain stable and are basically not affected by the bending curvature, which once again reflects the excellent bending resistance of [Ge(5 nm)/Sb(5 nm)]$_5$ multilayer films.

Microstructure characterization of flexible Ge/Sb films

In Fig. 3a, the [Ge(5 nm)/Sb(5 nm)]$_5$ multilayer film with PEEK as substrate is fixed at both ends, and the tension exerted on the film

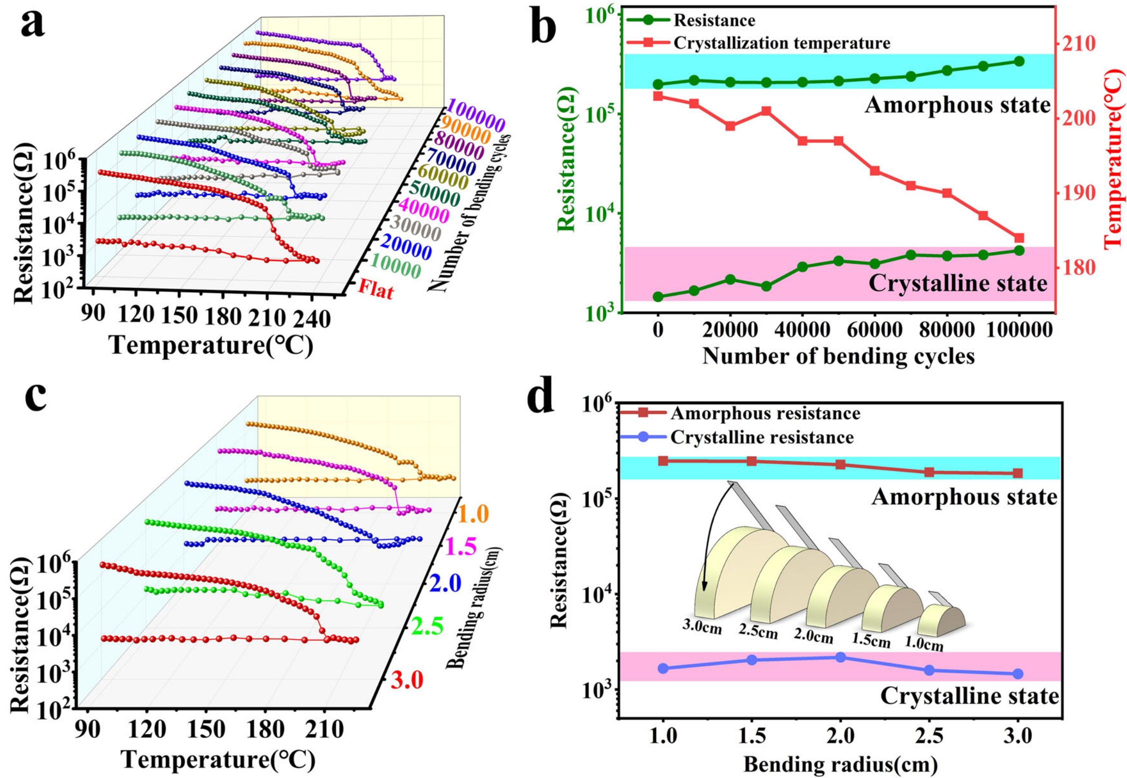

Fig. 2 Influence of bending number and bending radius on resistance of flexible thin films. a *R–T* graphs of [Ge(5 nm)/Sb(5 nm)]$_5$ multilayer films on a flexible PEEK substrate after different bending cycles. **b** Changes of the resistance and phase transition temperature after multiple bending. **c** *R–T* graphs of flexible [Ge(5 nm)/Sb(5 nm)]$_5$ multilayer films after bending 10,000 times on models with different bending radii. **d** The resistance change of the film after bending 10,000 times on different bending radius models. The illustration shows a schematic of the bending model.

by the tensile tester is tested by Newton force measurement. When no tension is applied, the length of the film is 2 cm. Figure 3b shows that the length of the film becomes 2.15 cm when a 100 N tension is applied with an elongation of 7.5%. Figure 3c shows the pressure process of [Ge(5 nm)/Sb(5 nm)]$_5$ multilayer film on PEEK substrate. Applying a pressure of 80 N to a square film with a side length of 1 cm, we can calculate that the pressure on the film is 8×10^{-4} Gpa.

Figure 3d shows the resistance drift of [Ge(5 nm)/Sb(5 nm)]$_5$ multilayer films on PEEK substrate. The resistance drift is mainly caused by internal defects in the film, and the power law equation is used to describe the resistance drift[38,39]:

$$R_t = R_0\left(\frac{t}{\tau_0}\right)\alpha \tag{1}$$

Where R_t represents the measurement resistance, R_0 and τ_0 are the initial constants, and α is denoted as the resistance drift coefficient. The α of the film are 0.00752 ± 0.00007, 0.00904 ± 0.00005, 0.00905 ± 0.00018 and 0.00899 ± 0.00009 after the film is bent 10,000 times, stretched 7.5% and compressed at 8 × 10^{-4} Gpa for 24 h, respectively. The smaller the film resistance drift coefficient is, the more beneficial it is to maintain the stability of the device resistance. The results show that, compared with the flat state, the α of the film increases slightly after multiple bending, stretching and pressure. This may be caused by the destruction of the internal structure under the action of stress.

Figure 3e shows the crystalline structure of [Ge(5 nm)/Sb(5 nm)]$_{50}$ multilayer films with PEEK as substrate by XRD testing. After annealing at 250 °C for 5 min, the film is bent 80,000 times, stretched 7.5% and compressed at 8 × 10^{-4} Gpa for 24 h, and then XRD is tested. It can be seen from the XRD pattern that the (012), (210) and (015) diffraction peaks belonging to Sb crystal phase appear in all the samples[40]. Sb material belongs to the nucleation dominated crystallization mechanism and has a fast phase transition rate. In [Ge(5 nm)/Sb(5 nm)]$_{50}$ films, the overall crystallization rate of the phase change films can be enhanced by incorporating a significant number of Sb layers. Moreover, the absence of any Ge phase in the diffraction pattern suggests that Ge is present in an amorphous state. Multilayer amorphous Ge can separate Sb, reduce phase transition region, inhibit grain growth, lower power dissipation and enhance thermostability of the film[41]. The diffraction pattern also shows that, compared with the flat state, the Sb (210) diffraction peak of the film is shifted to a higher angle after bending 80000 times, stretching and pressing, which is caused by the reduction of Sb lattice constant[42]. When the film is bent, the outer surface is in a stretched state, so the film is subjected to tensile stress during bending and stretching. The tensile stress can increase the strain of the grain boundary, causing the grain refinement[43]. When the film is subjected to compressive stress, the pressure provides additional strain energy, which promotes grain boundary migration and plastic deformation of the crystal, thus making the grain fine[44].

The resistance of semiconductor materials is significantly influenced by the energy band. In this paper, the reflectance spectra of thin films with wavelength range from 400 to 2500 nm have been measured by near infrared spectrophotometer. Figure 3f shows the band gap E_g of [Ge(5 nm)/Sb(5 nm)]$_{50}$ multilayer films after annealing at 250 °C for 5 min evaluated using the Kubelka-Munk (K–M) function, which is formulated as follows[45]:

$$\frac{K}{S} = (1-R)^2/(2R) \tag{2}$$

Where K denotes the absorption coefficient, R represents reflectivity, and S stands for scattering coefficient. The curve is normalized and fitted to the horizontal coordinate, and the energy intercept is the band gap E_g. The E_g of [Ge(5 nm)/Sb(5 nm)]$_{50}$ multilayer film on PEEK substrates are 1.325, 1.333, 1.337, 1.340, 1.339 and 1.338 eV for flat state, bending 20000, 40000, 80000

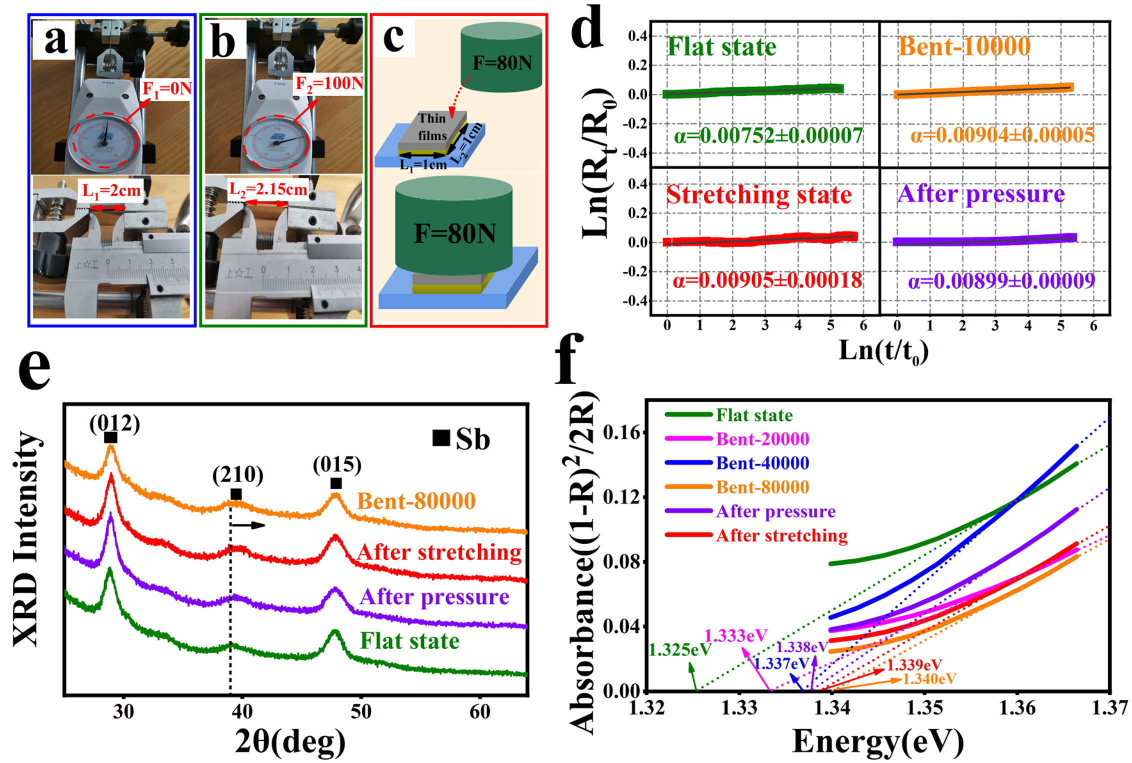

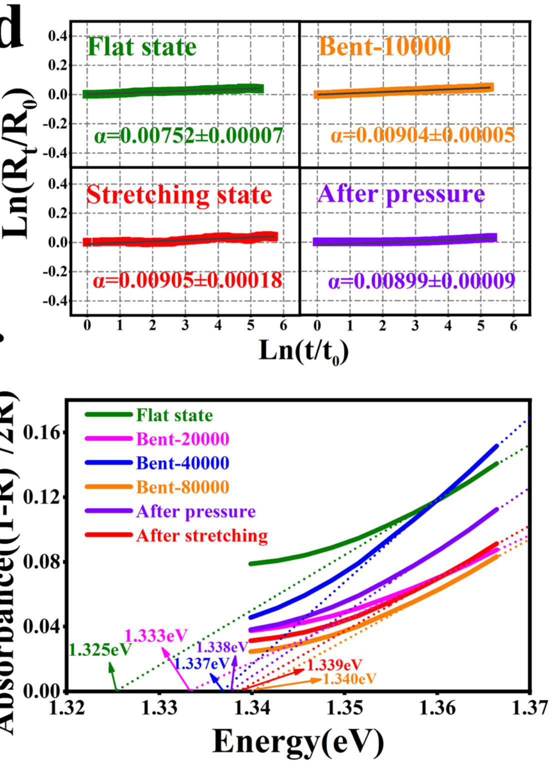

Fig. 3 Resistance drift, XRD and near infrared testing of Ge/Sb flexible films. **a**, **b** The length measurement of $[Ge(5\ nm)/Sb(5\ nm)]_5$ multilayer film with PEEK as the substrate film at 0 and 100 N tensile forces. **c** Film pressure process diagram. **d** Resistance drift of $[Ge(5\ nm)/Sb(5\ nm)]_5$ multilayer film with PEEK as substrate after flat, bending 10000 times, stretching and pressure states. **e** XRD pattern of $[Ge(5\ nm)/Sb(5\ nm)]_5$ on PEEK substrates in flat, bending 80,000 times, pressing and stretching states. **f** Kubelka-Munk function graphs of $[Ge(5\ nm)/Sb(5\ nm)]_5$ multilayer films in flat, after multiple bending, pressure and stretching states.

times, 7.5% stretching and compressed at 8×10^{-4} Gpa for 24 h, respectively. When the energy band is increased, the energy gap may become larger. Furthermore, an increased amount of energy is required for the electrons to undergo a transition from the valence band to the conduction band, so the resistivity may increase. After repeated bending, the energy gap of the film increases slightly, resulting in increased crystalline resistance, which aligns with the outcome depicted in Fig. 2b. The strain generated by the tensile stress will cause lattice distortion, which can change the shape of the band, thus leading to the increase of the band gap. Therefore, the energy band of the film after bending and stretching is greater than that of the flat state ($E_g \sim 1.325$ eV). Under the action of compressive stress, the distance between the atomic structure of the film material decreases, the overlap of the electron cloud increases, and the interaction between the charges is enhanced, resulting in the transition from ionic bond to covalent bond between the atoms, resulting in a larger band gap[46]. The relationship between the band $E_g(P)$ and the pressure $P(x)$ of the film material is as follows:

$$E_g(P) = E_g(0)\left[1 - \frac{1}{E_{b0}}\frac{V_0}{n}\int_1^x P(x)dx\right] \quad (3)$$

Where, $x = V/V_0$ represents the volume ratio after compression to before compression, V_0 represents the cell volume of the material at pressure of 0 Pa and temperature of 0 K, n is the number of bonds contained in the volume, and E_{b0} represents the single bond energy of the material at pressure of 0 Pa and temperature of 0 K. The pressure $P(x)$ is determined by the Birch-Murnaghan equation:

$$P(x) = \frac{3B_0}{2}\left(x^{-7/3} - x^{-5/3}\right)\left[1 + \frac{3}{4}\left(B_0' - 4\right)\left(x^{-2/3} - 1\right)\right] \quad (4)$$

Where B_0 is the bulk modulus of the material and B_0' is the first derivative of the bulk modulus with respect to pressure. According to the above formula, when the pressure increases, the bond length becomes shorter and the bond energy becomes stronger, causing the crystal potential energy to increase, so that the band gap exhibits a positive correlation with the rise in pressure. In this paper, the energy band ($E_g \sim 1.338$ eV) of the film under static pressure of 8×10^{-4} Gpa for 24 h is greater than that of the flat state ($E_g \sim 1.325$ eV), which is consistent with the above theory.

Surface roughness testing of flexible Ge/Sb films

The $[Ge(5\ nm)/Sb(5\ nm)]_{50}$ multilayer film with PEEK as the substrate is annealed for 5 min at 250 °C for AFM test, and the film's surface morphology is observed for flat state, multiple bending, 7.5% stretching and standing at 8×10^{-4} Gpa pressure for 24 h. Figure 4a, e, and i show the surface morphology of the film in flat state, after stretching and pressing. In the scanning range of 10 μm × 10 μm, it is observed that the film has no cracks on the surface after stretching and pressing, which reflects the good tensile and compressive properties of the film. Figure 4b, f, and j show the most probable height (MPH) of the film in flat state, after stretching and pressure. It can be seen that the MPH of the film in flat state, after stretching and pressure are 56.5, 41.3 nm and 49.5 nm, respectively, indicating that stretching and pressure lead to a reduction in the surface grain size of the film, resulting in a flatter surface.

The Gauss curvature K_G of the film surface is[47]:

$$K_G = \frac{a^2}{\left(a^2\sin^2\theta + b^2\cos^2\theta\right)^2} \quad (5)$$

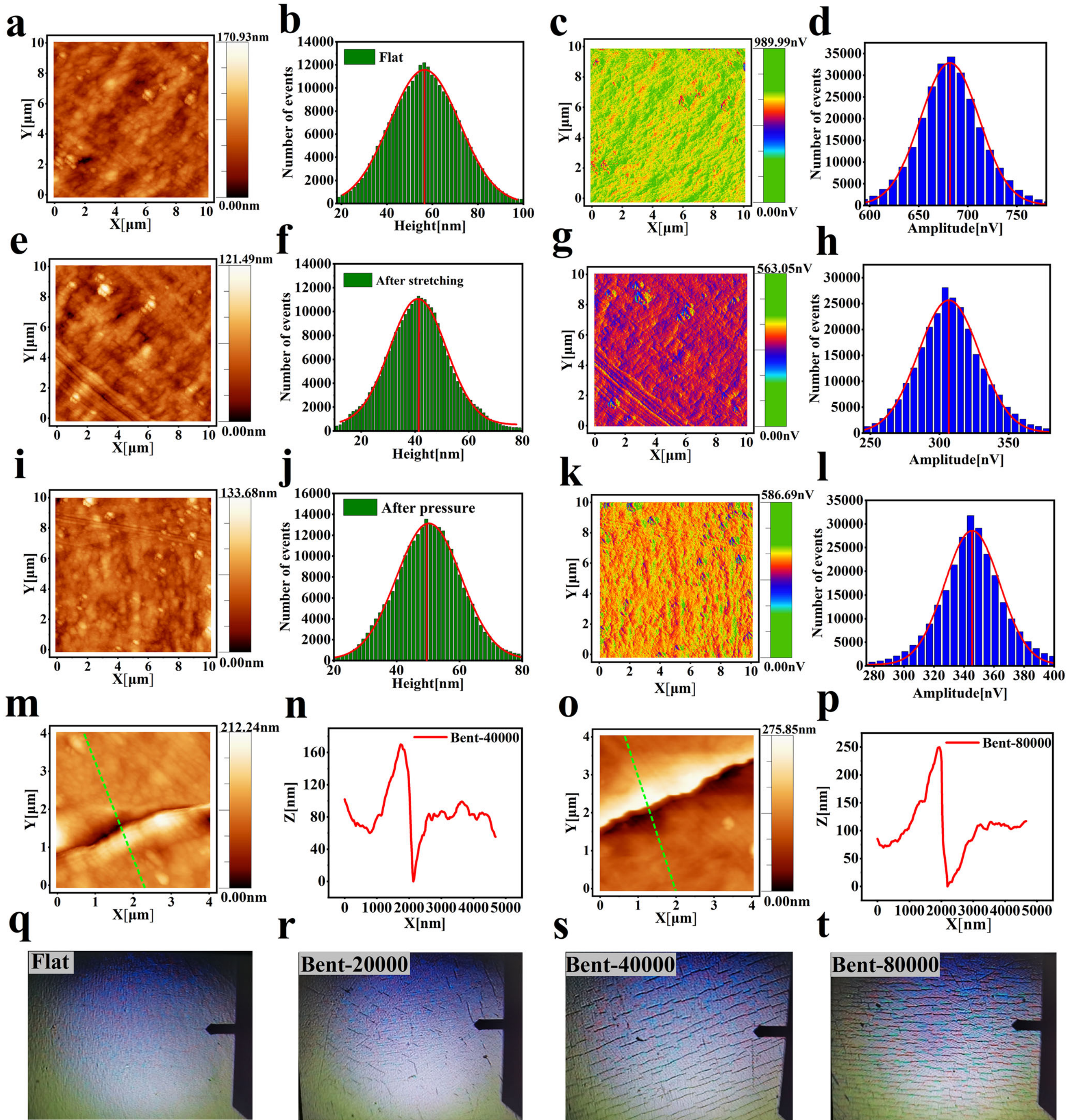

Fig. 4 Surface roughness of Ge/Sb flexible films. **a**, **e**, **i** Surface characteristics of $[Ge(5\ nm)/Sb(5\ nm)]_{50}$ multilayer films with PEEK as substrate for flat state, 7.5% stretching and pressure of 8×10^{-4} Gpa. **b**, **f**, **j** Histogram depicting the distribution of surface height for the film in flat state, after stretching and pressure. **c**, **g**, **k** Electrostatic potential distribution on the surface of the film, after stretching and pressure. **d**, **h**, **l** Histogram depicting distribution of surface electrostatic potential for the film in flat state, after stretching and pressure; **m** and **o** Surface morphologies of the film after bending 40,000 and 80,000 times. **n** *Z*–*X* curve of the green line region in (**m**). **p** *Z*–*X* curve of the green line region in (**o**). **q**–**t** Surface appearance of the film in a flat state, after bending 20,000, 40,000 and 80,000 times (magnified 200 times).

For a given electric charge Q, the charge density σ within an ellipsoid is[48]:

$$\sigma \frac{Qa^2}{4\pi b\left(a^2\sin^2\theta + b^2\cos^2\theta\right)^{1/2}} \tag{6}$$

Where a and b are constants, we get ${K_G}^{1/4} \propto \sigma$. Therefore, the electric potential $U \propto \sigma$ near the surface can be used to accurately analyze the surface topography and conductivity of the film through the electrostatic potential of the surface. Figure 4c, g, and k show the surface electrostatic potential distribution of the film in flat state, after stretching and pressure, respectively. The surface charge concentration of the film after stretching and pressing is significantly lower than that in flat state. Figure 4d, h, and l show the histogram of surface potential distribution of the film in flat state, after stretching, and pressure conditions. The most probable potential (MPP) of the film after stretching and pressure are 306

and 345 nV, respectively, which are smaller than the MPP of the film in the flat state (~682 nV), indicating that the surface particle curvature of the film is significantly reduced after stretching and pressure, and the overall flatness of the film's surface is improved, which is in agreement with the findings from the XRD analysis depicted in Fig. 3e.

Figure 4m and o show the surface morphologies of the film with bending 40,000 and 80,000 cycles in the scanning range of 4 μm × 4 μm, respectively. Cracks appeared on the surface of the film after 40,000 and 80,000 cycles of bending. In Fig. 4n and p, *Z*–*X* diagrams of the green line region in Fig. 4m and o are shown respectively, where *X* represents the distance of the horizontal plane of the film and *Z* represents the distance perpendicular to the surface of the film. The width and depth of cracks on the surface of the film are measured according to the horizontal distance and vertical distance in the *Z*–*X* diagram. After the film is bent for 40,000 times, the surface crack width was about 557 nm and the depth is about 83 nm. After the film is bent 80000 times, the surface crack width is about 1086 nm, and the depth is about 108 nm. It can be concluded that the more bending cycles, the larger the surface crack size of the film.

Figure 4q–t show the surface appearance of the film in flat state, after 20,000, 40,000 and 80,000 bending times, respectively. It is evident from the diagram that cracks appear after multiple bending of the film. With the increase of bending times, the size and number of micro-cracks on the surface of the film also increase. The stress field intensity factor *K* can reflect the magnitude of the stress concentration near the tip of the crack. The factor *K* that characterizes the intensity of the stress field is[49]:

$$K = \sigma\sqrt{\pi a} \tag{7}$$

Where σ represents the stress, a is the crack size, and the factor K is proportional to the stress and crack size. When the film is subjected to stress, the surface of the film will produce stress concentration effect, resulting in the formation of cracks. The small crack size will cause the stress field to concentrate in the local crack area and accelerate the crack propagation. With the increase of crack size, the stress field may be widely concentrated, and the stress concentration will accelerate the creation and dissemination of fissures. Therefore, as the number of bending cycles of the film increases, cracks on the surface of the film expand, and the size and number of cracks increase accordingly, which is aligns with the findings presented in Fig. 2b. The crack fatigue fracture process consists of three stages: crack initiation stage, crack expansion stage and instantaneous fracture stage. After microcracks appear on the surface of the film, the electrical conductivity of the film becomes worse, so the resistivity will increase. With the increase of the number of bending cycles, the small micro-cracks on the surface of the film will be subjected to stress concentration effect, which will accelerate the generation and diffusion of cracks, further reduce the conductivity of the film, and thus increase the resistivity. It can be seen from the figure that the surface of the film does not fracture after multiple bending, which reflects the film exhibits excellent resistance to fatigue caused by bending.

Device fabrication and electrical performance test

PCM devices based on $[Ge(5\,nm)/Sb(5\,nm)]_8$ multilayer films are fabricated on flexible PEEK substrate. The electrical properties of these devices were tested in various state, including a flat state, a bent state, and after undergoing 1000 bending cycles. Figure 5a depicts the fabrication process of the PCM device. Initially, a 150 nm layer of Ag is sputtered onto the PEEK substrate as the bottom electrode. This bottom electrode is then covered with a mask, through which the intermediate phase change layer material and a 225 nm layer of top electrode (Ag) are sputtered via fine holes in the mask. PCL refers to Ge/Sb multilayer thin film structure. After completing this deposition process, the mask plate is removed. Figure 5b shows an image of the PCM device in its bent state along with an enlarged view of its surface electrode morphology. Figure 5c illustrates *I*–*V* curves for the PCM device under different conditions: flat state, bent state, and after being subjected to 1000 bending cycles. As voltage increases during scanning, so does current flow. Once voltage reaches threshold voltage V_{th}, there is a sharp decrease in voltage accompanied by rapid increase in current until it stabilizes at low resistance state indicating amorphous to crystalline transition of film occurs. This negative resistance phenomenon can be observed from the figure, the threshold voltages of the film in flat state, bent state and after being subjected to 1000 bending cycles are 1.05, 2.02 and 2.25 V respectively, which means that bending will increase the operating power consumption of the device[50].

Figure 5d, e, and f show the *R*–*V* curves of the PCM device based on the flexible $[Ge(5\,nm)/Sb(5\,nm)]_8$ multilayer film on PEEK substrate in flat state, bending state, and after bending 1000 times, respectively. The film can achieve reversible SET-RESET transformation at 100 and 10 ns pulse widths in flat state, bent state and after bending 1000 times. The high and low resistances are more than two orders of magnitude, ensuring that the resistance state can be effectively identified. It is worth noting that the film in flat state can achieve reversible SET-RESET operation at a pulse width of 6 ns, indicating that the $[Ge(5\,nm)/Sb(5\,nm)]_8$ multilayer film device with PEEK as the substrate has ultra-fast phase transition speed.

We try to test the electrical conversion performance in the bending state of the device and after bending 1000 times at the pulse width of 6 ns, but the reversible operation of SET-RESET could not be achieved. This may be because the internal microstructure of the device is affected after bending, such as defects and micro-cracks. This damages the electrical performance of the device to some extent. However, the device can achieve SET-RESET reversible operation at a pulse width of 10 ns both in the bending state and after 1000 times of bending, indicating that the device still has ultra-fast phase transition speed in the bending state and after 1000 times of bending. The practicability of Ge/Sb multilayer films on PEEK substrate in future high-performance flexible memory devices is further verified.

We compare the properties of Ge/Sb phase change films on Si substrates and PEEK substrates. The crystalline resistance of Ge/Sb devices based on Si substrate and PEEK substrate is about 2×10^4 Ω at 10 ns pulse width, and there is little difference between the two[51]. The V_{RESET} of Ge/Sb devices based on Si substrate and PEEK substrate at 10 ns pulse width is 3.15 and 4.23 V, respectively. According to V_{RESET}, the power consumption of the FPCM device during RESET operation can be evaluated[52]:

$$E_{\mathrm{RESET}} = V_{RESET}^2 \times \frac{t}{R_{SET}} \tag{8}$$

E_{RESET} refers to the power consumption generated during the RESET process, V_{RESET} is the voltage during the RESET process, t is the pulse width, and R_{SET} is the crystalline resistance. According to the formula, the RESET operating power consumption of Ge/Sb devices on Si substrate and PEEK substrate is 4.96×10^{-12} and 8.95×10^{-12} J respectively, so the power consumption of Ge/Sb multilayer films on PEEK is slightly higher than that on Si substrate. In this paper, we have verified that Ge/Sb multilayer phase change films can achieve phase change on PEEK substrate, and have ultra-fast phase change speed and bending fatigue resistance. Therefore, we believe that flexible Ge/Sb phase change films based on PEEK substrate have a good application prospect.

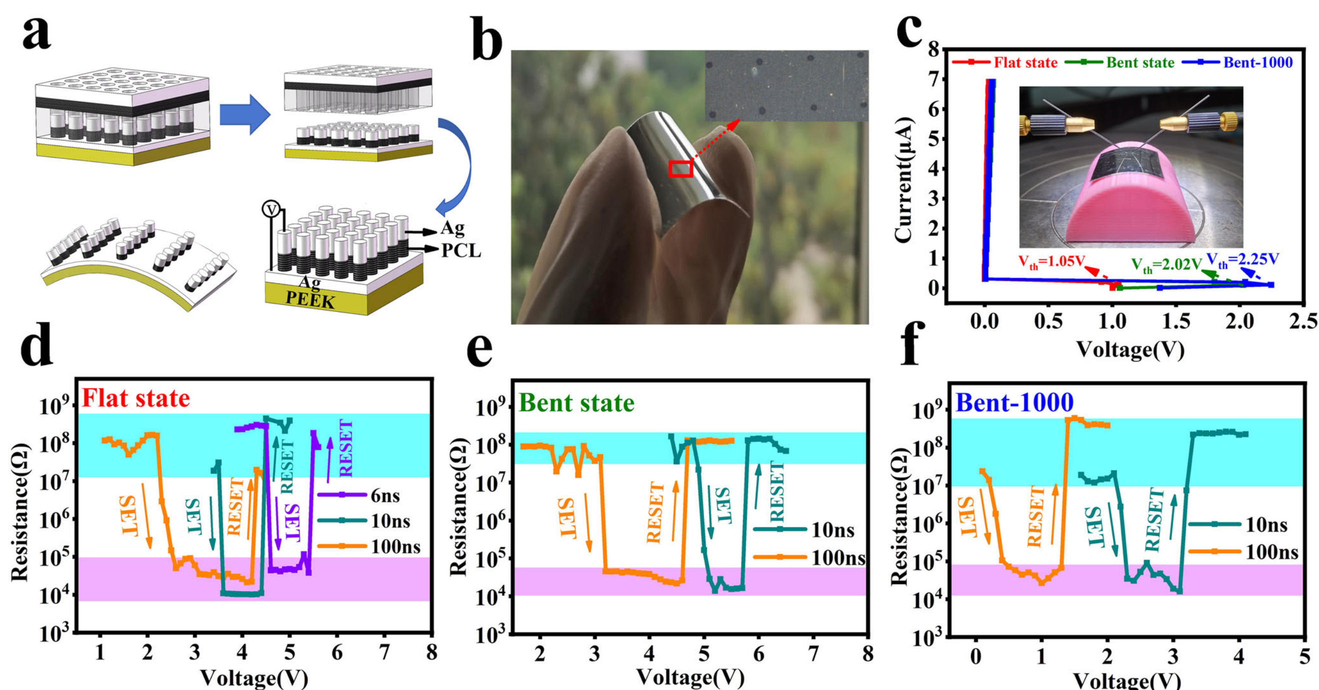

Fig. 5 Electrical properties testing of flexible Ge/Sb films. **a** Process for preparing flexible PCM devices based on $[Ge(5\ nm)/Sb(5\ nm)]_8$ multilayer films. **b** Physical drawings depicting PCM devices in a flexed condition and morphology of electrodes on the surface. **c** *I*–*V* curves of the film in flat state, bending state and after bending 1000 times, illustration is the test diagram of the device in bending state. **d**–**f** Are *R*–*V* curves of the film in flat state, bending state and after bending 1000 times respectively.

DISCUSSION

In this paper, Ge/Sb multilayer films were prepared on flexible PEEK substrate by magnetron sputtering technology. The findings indicated that the phase transformation of Ge/Sb multilayer films on PEEK substrate is feasible. After the composite with Ge material, the thermal stability of Sb film can be improved with the T_c 203 °C. The amorphous and crystalline resistances of $[Ge(5\ nm)/Sb(5\ nm)]_5$ multilayer films tend to increase after several bending cycles, and the T_c decreases. After the film was bent several times at different bending radius, the amorphous and crystalline resistances maintained a fairly consistent level. Bending, stretching and pressure can result in grain refinement. Cracks will occur on the surface of the film after bending many times, and the film's surface achieves a higher level of smoothness after stretching and pressure. The flexible device based on $[Ge(5\ nm)/Sb(5\ nm)]_8$ multilayer film can achieve reversible SET-RESET transition operation under an ultrashort pulse width of 6 ns. The results show that Ge/Sb multilayer film based on flexible PEEK substrate has good resistance to bending, stretching and compression, and have the potential to evolve into a future high-performance phase-change memory.

METHODS

Films preparation

The method of alternating sputtering with Ge and Sb targets was used to prepare multilayer films of Ge/Sb and pure Sb on a PEEK substrate. The purity level of the Ge and Sb targets was 99.999%. A sputtering power of 30 W was applied, while the sputtering time was calculated based on the target's speed to control film thickness. In order to avoid any impact from varying thickness, all films were set to have a total thickness of 50 nm. Prior to sputtering, argon gas was injected at a controlled flow rate of 30 SCCM. The sputtering pressure was maintained at 0.4 Pa, with the vacuum chamber's limit pressure kept at 4 × 10–4 Pa for consistency. To ensure uniform deposition across the film surface, the sample disk rotation rate was controlled at 20 r/min.

Characterization

The resistance-temperature curves were measured by a hot and cold table test system, and the resistance drift index was calculated. Crystal phase structure analysis after bending, stretching, and compressing experiments was conducted using an X-ray diffractometer. Diffuse reflectance spectra in the wavelength range of 400–2500 nm were recorded using a near-infrared spectrophotometer. Atomic force microscopy (AFM) observations were made to examine surface morphology and electrostatic potential variations in the films. PCM devices based on Ge/Sb multilayer films on PEEK substrate were fabricated for further testing electrical properties in flat state, bent state, and after multiple bends using Keithley 2400 series digital source meter combined with Tektronix AWG5012C series.

DATA AVAILABILITY

All data generated or analysed during this study are included in this published article.

Received: 20 August 2023; Accepted: 18 January 2024;
Published online: 31 January 2024

REFERENCES

1. Carbone, M. NiO-based electronic flexible devices. *Appl. Sci.* **12**, 2839 (2022).
2. Gong, M., Zhang, L. & Wan, P. Polymer nanocomposite meshes for flexible electronic devices. *Prog. Polym. Sci.* **107**, 101279 (2020).
3. Tao, L. et al. Fabrication techniques and applications of flexible graphene-based electronic devices. *J. Semicond.* **37**, 041001 (2016).
4. Han, S. T., Zhou, Y. & Roy, V. A. Towards the development of flexible non-volatile memories. *Adv. Mater.* **25**, 5425–5449 (2013).
5. Chen, Z. et al. Advanced flexible materials from nanocellulose. *Adv. Funct. Mater.* **33**, 2214245 (2023).

6. Kanahashi, K., Pu, J. & Takenobu, T. 2D Materials for large-area flexible thermoelectric devices. *Adv. Energy Mater.* **10**, 1902842 (2019).
7. Khan, A. I. et al. alow-switching current density multilevel phase-change memory on a flexible substrate. *Science* **373**, 1243–1247 (2021).
8. Pendergraph, S. A., Bartlett, M. D., Carter, K. R. & Crosby, A. J. Opportunities with fabric composites as unique flexible substrates. *ACS Appl. Mater. Interfaces* **4**, 6640–6645 (2012).
9. Zhou, Z., Zhang, H., Liu, J. & Huang, W. Flexible electronics from intrinsically soft materials. *Giant* **6**, 100051 (2021).
10. Guo, R. et al. Non-volatile memory based on the ferroelectric photovoltaic effect. *Nat. Commun.* **4**, 1990 (2013).
11. Wang, K. L., Alzate, J. G. & Khalili, P. Low-power non-volatile spintronic memory: STT-RAM and beyond. *J. Phys. D Appl. Phys.* **46**, 074003 (2013).
12. Lu, Y. G. et al. Mixed-mode operation of hybrid phase-change nanophotonic circuits. *Nano Lett.* **17**, 150–155 (2017).
13. Bez, R., Camerlenghi, E., Modelli, A. & Visconti, A. Introduction to flash memory. *IEEE* **91**, 489–502 (2003).
14. Burr, G. W. et al. Phase change memory technology. *J. Vac. Sci. Technol. B.* **28**, 223–262 (2010).
15. Pan, F., Gao, S., Chen, C., Song, C. & Zeng, F. Recent progress in resistive random access memories: materials, switching mechanisms, and performance. *Mat. Sci. Eng. R.* **83**, 1–59 (2014).
16. Vincent, A. F. et al. Spin-transfer torque magnetic memory as a stochastic memristive synapse for neuromorphic systems. *IEEE T. Biomed. Circ. S.* **9**, 166–174 (2015).
17. Ni, K. et al. Critical role of interlayer in $Hf_{0.5}Zr_{0.5}O_2$ ferroelectric FET nonvolatile memory performance. *IEEE T. Electron Dev.* **65**, 2461–2469 (2018).
18. Cao, T., Lian, M., Chen, X. Y., Mao, L. B. & Liu, K. et al. Multi-cycle reconfigurable THz extraordinary optical transmission using chalcogenide metamaterials. *Opto-Electron. Sci* **1**, 210010 (2022).
19. Li, J. & Lam, C. Phase change memory. *Sci. China Inf. Sci.* **54**, 1061–1072 (2011).
20. Ohta, T. Phase change memory and breakthrough technologies. *IEEE T. Magn.* **47**, 613–619 (2011).
21. Bao, J. X. et al. Nonvolatile chirality switching in terahertz chalcogenide metasurfaces. *Microsyst. Nanoeng.* **8**, 112 (2022).
22. Ghazi Sarwat, S. et al. Projected mushroom type phase-change memory. *Adv. Funct. Mater.* **31**, 2106547 (2021).
23. Yoon, S. M. et al. Time dependent resistance change of amorphous phase in phase-change nonvolatile memories. *Integr. Ferroelect.* **93**, 83–89 (2010).
24. Liu, B. et al. Universal memory based on phase-change materials: from phase-change random access memory to optoelectronic hybrid storage. *Chin. Phys. B* **30**, 058504 (2021).
25. Zhang, S. J. et al. Nonvolatile reconfigurable terahertz wave modulator. *Photonix* **3**, 7 (2022).
26. Du, T., Han, X., Yan, X., Shang, J., Li, Y. & Song, J. MXene-based flexible sensors: materials, preparation, and applications. *Adv. Mater. Technol.* **8**, 2202029 (2023).
27. Li, Y. et al. High-efficiency robust perovskite solar cells on ultrathin flexible substrates. *Nat. Commun.* **7**, 10214 (2016).
28. Muralee Gopi, C. V. V., Vinodh, R., Sambasivam, S., Obaidat, I. M. & Kim, H. J. Recent progress of advanced energy storage materials for flexible and wearable supercapacitor: from design and development to applications. *J. Energy Storage* **27**, 101035 (2020).
29. Palchoudhury, S., Ramasamy, K., Gupta, R. K. & Gupta, A. Flexible supercapacitors: a materials perspective. *Front. Mater.* **5**, 00083 (2019).
30. Zhang, Y., Zhang, T., Huang, Z. & Yang, J. A new class of electronic devices based on flexible porous substrates. *Adv. Sci.* **9**, e2105084 (2022).
31. Yadav, P., Singhal, S. & Patra, A. Electropolymerized poly(3,4-ethylenedioxyselenophene) on flexible substrate: a comparative study of electronic and electrochromic properties with sulfur analogue and rigid substrate. *Synth. Met.* **260**, 116264 (2020).
32. Pal, A. et al. Synthesis and characterization of Sr-doped HAp-incorporated polyether ether ketone composite. *J. Compos. Mater.* **54**, 287–298 (2019).
33. Yang, J. et al. Microcellular injection molding of polyether-ether-ketone. *Polymer* **251**, 124866 (2022).
34. Xu, J. & Hu, Y. Stability enhancement and resistance drift suppression of antimony thin films by hafnium oxide interlayers. *J. Mater. Res. Technol.* **18**, 4631–4440 (2022).
35. Hu, Y. F., Lai, T. S., Di, C. & Yan, X. The coupling effect and phase transition behavior of multiple interfaces in GeTe/Sb superlattice-like films. *J. Alloy Compd.* **871**, 159467 (2021).
36. Hu, Y. F., You, H. P., Chou, Q. & Lai, T. S. Regulating phase change behavior and surface characteristicsof Sn15Sb85 thin film by oxygen doping. *J. Phys. D Appl. Phys.* **52**, 415104 (2019).
37. Yu, Z., Li, Y. Q., Xia, F. & Xue, W. The characteristics of indium tin oxide films prepared on various buffer layer-coated polymer substrates. *Surf. Coat. Tech.* **204**, 131–134 (2009).
38. Wu, X. et al. Understanding Interface-controlled resistance drift in superlattice phase change memory. *IEEE Electr. Device L.* **43**, 1669–1672 (2022).
39. Zhou, L. et al. Resistance drift suppression utilizing $GeTe/Sb_2Te_3$ superlattice-like phase-change materials. *Adv. Electron Mater.* **6**, 1900781 (2019).
40. Zhu, X. Q. et al. Si/Sb superlattice-like thin films for ultrafast and low power phase change memory application. *Scr. Mater.* **121**, 66–69 (2016).
41. Yoo, Y. G., Yang, D. S., Ryu, H. J., Cheong, W. S. & Baek, M. C. Local structural and optical properties of GeSb phase-change materials. *Mater. Sci. Eng. A* **449**, 627–630 (2007).
42. Liu, L. et al. Dependences of the oxygen reduction reaction activity of Pd–Co/C and Pd–Ni/C alloy electrocatalysts on the nanoparticle size and lattice constant. *Top. Catal.* **57**, 595–606 (2013).
43. Lu, L., Shen, Y., Chen, X., Qian, L. & Lu, K. Ultrahigh strength and high electrical conductivity in copper. *Science* **304**, 422–426 (2004).
44. Bobylev, S. V. & Ovid'ko, I. A. Stress-driven migration of deformation-distorted grain boundaries in nanomaterials. *Acta Mater.* **88**, 260–270 (2015).
45. Landi, S. et al. Use and misuse of the Kubelka-Munk function to obtain the band gap energy from diffuse reflectance measurements. *Solid State Commun.* **341**, 114573 (2022).
46. Ramzan, M., Hussain, T. & Ahuja, R. High pressure phase determination and electronic properties of lithiumamidoborane. *Appl. Phys. Lett.* **101**, 111902 (2012).
47. Puglisi, G. & Zurlo, G. Electric field localizations in thin dielectric films with thickness non-uniformities. *J. Electrostat.* **70**, 312–316 (2012).
48. Curtright, T. L. et al. Charged line segments and ellipsoidal equipotentials. *Eur. J. Phys.* **37**, 035201 (2016).
49. Sun, C. T. & Qian, H. Y. Brittle fracture beyond the stress intensity factor. *J. Mech. Mater. Struct.* **4**, 743–753 (2009).
50. Gan, K. J. & Liang, D. S. Investigation of adjustable current-voltage characteristics and hysteresis phenomena for multiple-peak negative differential resistance circuit. *IEICE T. Electron.* **E93-C**, 514–520 (2010).
51. Chen, S., Yang, K., Wu, W., Zhai, J. & Song, Z. Superlattice-like Sb-Ge thin films for high thermal stability and low power phase change memory. *J. Alloy. Compd.* **738**, 145–150 (2018).
52. Gao, S. W., Hu, Y. F., Cao, L. W. & Zhu, X. Q. Study on the performance of flexible memory device based on antimony film. *IEEE Electron. Device Lett.* **44**, 392–395 (2023).

ACKNOWLEDGEMENTS

This work was supported by National Natural Science Foundation of China (No. 11974008) and the Open Project Program of Shanxi Key Laboratory of Advanced Semiconductor Optoelectronic Devices and Integrated Systems (No. 2023SZKF20) and Postgraduate Research and Practice Innovation Program of Jiangsu University of Technology (XSJCX23_26).

AUTHOR CONTRIBUTIONS

Y.H. conceived the research. C.W. and Y.H. conceived the idea and designed the experiment. C.W. performed device fabrication with help from Y.H. and contributed to data collection. Y.H. and L.L. obtained the funding. C.W. wrote the whole paper. Y.H. reviewed the paper. All the authors gave valuable comments on this paper.

COMPETING INTERESTS

The authors declare no competing interests.

ADDITIONAL INFORMATION

Correspondence and requests for materials should be addressed to Yifeng Hu.

Reprints and permission information is available at http://www.nature.com/reprints

Publisher's note Springer Nature remains neutral with regard to jurisdictional claims in published maps and institutional affiliations.

Open Access This article is licensed under a Creative Commons Attribution 4.0 International License, which permits use, sharing, adaptation, distribution and reproduction in any medium or format, as long as you give appropriate credit to the original author(s) and the source, provide a link to the Creative Commons license, and indicate if changes were made. The images or other third party material in this article are included in the article's Creative Commons license, unless indicated otherwise in a credit line to the material. If material is not included in the article's Creative Commons license and your intended use is not permitted by statutory regulation or exceeds the permitted use, you will need to obtain permission directly from the copyright holder. To view a copy of this license, visit http://creativecommons.org/licenses/by/4.0/.

© The Author(s) 2024